processes

MDPI

Article

Three-Dimensional Analysis of the Flow Characteristics Induced by a Cubic Artificial Reef with Diversions

Haiying Mao [1],*, Ziyi Wang [2], Cong Hu [3] and Kairui Wang [2]

1   College of Civil Engineering, Guangxi University of Science and Technology, Liuzhou 545006, China
2   College of Engineering, Ocean University of China, Qingdao 266100, China
3   China Renewable Energy Engineering Institute, Beijing 100120, China
*   Correspondence: 100002446@gxust.edu.cn

Abstract: In this paper, the flow characteristics induced by a cubic artificial reef with diversions (DCAR) were investigated using computational fluid dynamics (CFD). The results showed that the design of a DCAR can greatly improve the flow field range compared to typical cubic artificial reefs. The upwelling volume of the DCAR was more than 16 times that of a typical cubic artificial reef. The flow field effect produced the best results when the cut-opening ratio (COR) was 0.1–0.2 with constant flow. The parameters of the upwelling and back vortex increased with an increase in the flow velocity, and it decreased with an increase in the COR. The drag coefficient was less affected by the flow velocity, which remained between 1.32 and 1.44. The new type of artificial reef can improve the flow characteristics around the reefs.

Keywords: cubic artificial reef with diversion; three-dimensional analysis; flow velocity; cut-opening ratio; flow characteristics

1. Introduction

Nowadays, global coastal ecosystems are suffering from a series of problems such as environmental pollution, natural habitat destruction and overfishing. Lots of original coastal habitats are no longer suitable for fish to inhabit, resulting in a sharp decline in fishing resources. However, the application of artificial reefs can promote the development of fisheries. A marine engineering construction known as an artificial reef is used to enhance and repair the ecological environment in natural bodies of water [1–4]. Artificial reefs may draw and concentrate fish to increase the availability of certain fish [5–7]. To protect marine ecosystems and promote fishing at the same time, we need to propose new solutions, such as installing artificial reefs specifically designed for certain marine species [8]. Research found that fish species and production increased when artificial reefs were introduced. Furthermore, seaweed also doubled, which can help purify seawater. The artificial reefs placed in seawater can create an ecosystem, and thus improve the productivity of the sea area [9,10].

In recent years, numerous artificial reefs of various types and shapes, including the cube reef [11,12], Mi zi reef [13], truncated-cone-shaped reef [14], and trapezoid reef [15], have been created. Although the reefs have different shapes, they have some common features. For example, complicated structures can assist with the creation of turbulent flow, and the larger surface area can promote the formation of seaweed beds, which can supply more food for fish.

The main methods used in studies on the hydrodynamics of artificial reefs include numerical simulations and experiments. The foundation for the numerical simulations is computational fluid dynamics (CFD), and experiments mainly use particle image velocimetry (PIV) technology. The influence of the cut-opening ratio (COR) [16,17], cut-opening diameter [18], and layout-spacing [19,20] on the scale of the upwelling and vortices were

analyzed using CFD. The hydrodynamic phenomena surrounding single and double artificial trapezoidal reefs were investigated systematically using a series of 3D numerical values. The data show that the attack angle and opening ratio can significantly influence an artificial reef's hydrodynamic characteristics [21].

To study the force on the reef caused by the wave–current, a multifunctional 3D-numerical wave–current tank was built. The simulation results reveal that the flow field effect is greatest when there is a wave–current interaction, and a large vortex is formed at the back of the reef [22]. To study the effects of the opening factors on the flow field, methods of CFD and orthogonal experimental design were used. According to the findings, cut-opening shape and cut-opening ratio (OR) were key influencing factors [23]. We have constructed symmetrical reef models to examine their flow fields, and we used the computational fluid dynamics (CFD), a flow simulation approach, to reflect the influence of the void space complexity on the model. The efficiency indices of the upwelling and wake regions around the fractal triangle artificial reef model are 2–3 times higher than those of the fractal cube model [24]. The proposed solution was analyzed through CFD and the finite element method (FEM). As concrete was the base material for the artificial reefs, we tested four different water–cement ratios for the concrete mix. [25].

In the early days of studying an artificial reef's impact on the adjacent flow field, researchers preferred to use physical experiments including wind tunnel experiments and water tank experiments based on particle image velocimetry (PIV) technology. Wind tunnel experiments are used to study the impact of a reef's flow field formation by simulating the flow field with wind as the medium. In wind tunnel studies, the effects of square, pyramidal, and trigonal-shaped artificial reefs on the flow field were examined, and the amount and strength of the back wake and upwelling were measured. Compared with wind tunnel experiments, water tank experiments can better reproduce the working conditions of artificial reefs on the seafloor and objectively measure the flow field effects. Therefore, water tank experiments are often used to analyze the flow field effects, and the PIV technique is the primary tool for the study of the flow field [26]. The effects of side plates on the flow field of prismatic reefs were studied. According to the results, side plates can enhance the upwelling effect. Zhang et al. conducted flume experiments to determine the resistance and lateral force of four types of artificial reefs with different attack angles, reporting that the attack angle had a large effect on the resistance of the reef [27]. Fu et al. investigated how the opening rate affected the flow field of artificial reefs using PIV technology [28]. The study of artificial reefs focuses primarily on how the flow field varies along with the current velocity, reef shape, inflow angle, and the ecology around the reef. However, in deep ocean, the height and horizontal span of the upwelling may also affect the results.

As a result, this paper presents a new type of reef, evaluating its flow properties and stability at various CORs and flow velocities. CORs and flow velocities were investigated for their effects on upwelling and back vortex features. The paper is organized as follows: Section 2 describes the details of the numerical method. Section 3 analyzes the results, and Section 4 discusses the conclusion.

2. Materials and Methods

In this article, the simulation analysis is the main method of hydrodynamic characterization of artificial reefs, but experiments were designed to verify the reliability of the numerical flume. Because there was no PIV device in the laboratory, only flow velocity was compared between the numerical flume and experiments. Sections 2.1 and 2.2 introduce the design of the experiment, and Section 2.3 gives the details of the numerical model, such as the governing equations and turbulence model, structure of the artificial reef and the computational domain and grid convergence verification. Finally, Section 2.3.4 provides a comparison of the flow velocity between the simulation and experiments with different reef flow velocities and opening ratios.

2.1. Target Artificial Reef Experiment

The target artificial reef comprises a cubic frame and two upwelling plates which form the main body, as shown in Figure 1. The cubic frame has dimensions of $3 \times 3 \times 3$ m and a thickness of 0.2 m. The upwelling plates slope at 45°. Each blade has holes of equal diameter.
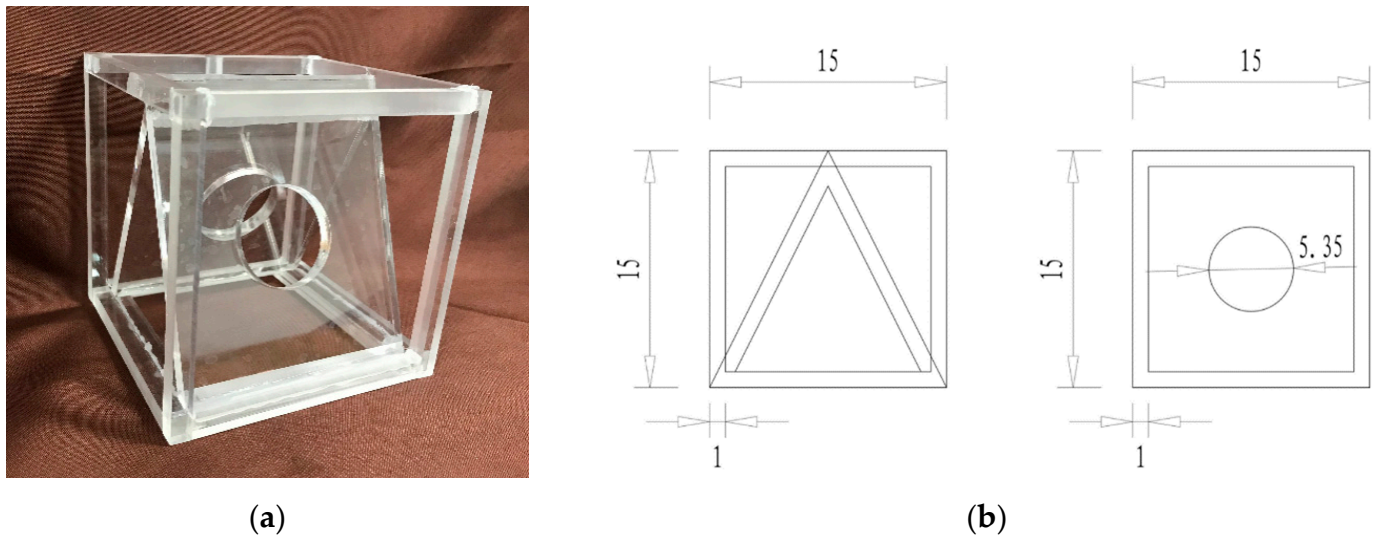

(a)

(b)

Figure 1. Model of the cubic artificial reef with diversions. (**a**) Model of the artificial reef. (**b**) Structure size of the model (unit: cm).

The material of the artificial reefs is concrete, and the concrete roughness is $n_a = 0.014$. If the scale of the experiment is $\lambda = 20$, then the model roughness $n_m = \frac{n_a}{\lambda^{1/6}} = 0.0085$. Moreover, the roughness of Plexiglas is 0.0070–0.0087, which meets the experimental requirements. The experimental reef model is depicted in Figure 1, and the dimensions of the outer boundary of the experimental reef are 0.15 m $\times$ 0.15 m $\times$ 0.15 m; the inverted V-shaped deflector and the frame both have a thickness of 0.01 m.

2.2. Experimental Apparatus and Method

The test was performed in the laboratory of the Ocean University of China in a two-dimensional current tank. The tank had a length, width, and depth of 4 m, 1.2 m, and 1 m, respectively. A pump at the end of the flume created a constant current. The pump's rotation frequency can be changed to produce various velocities. The tank's bottom and side walls are both composed of slick glass with very little frictional force.

One screw with a length of 2 m and diameter of 1 cm was connected to the dynamometer at one end, and its other end was connected to the DCAR. The DCAR was placed vertically in the center of the tank, and a small gap was left at the bottom of the tank (to avoid affecting the value of the dynamometer) (Figure 2). The flow velocity was measured with a Vectrino placed 0.6 m in front of the reef. The detector of the Vectrino was placed vertically above the center of the reef. The flow velocity at every point was measured three times and the average value was considered as the final value when the flow velocity was steady.

According to the gravity similarity criterion, when the flow velocities in the sea were 0.6 and 0.8 m/s, the velocities in the experiment were 0.134 and 0.178 m/s, respectively. First, the speed of the flow in front of the reef was made sure to be steady. Next, the velocity of A_1B_1 (coordinates of the measured point), A_2B_1, A_3B_1, A_4B_1, A_5B_1, and A_6B_1 were measured for every 15 s. The locations of the measurement points around the DCAR model are depicted in Figure 3.
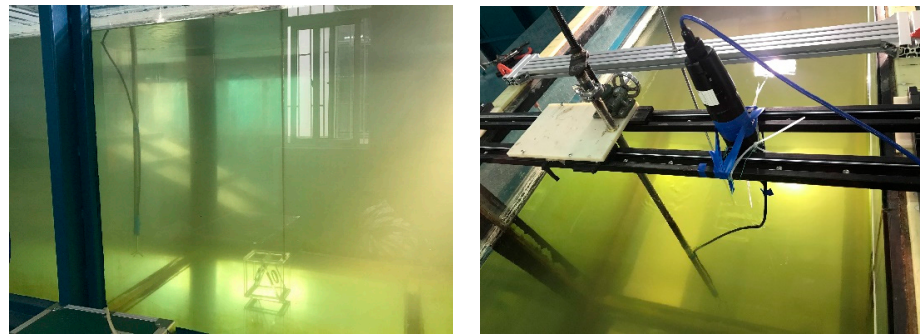
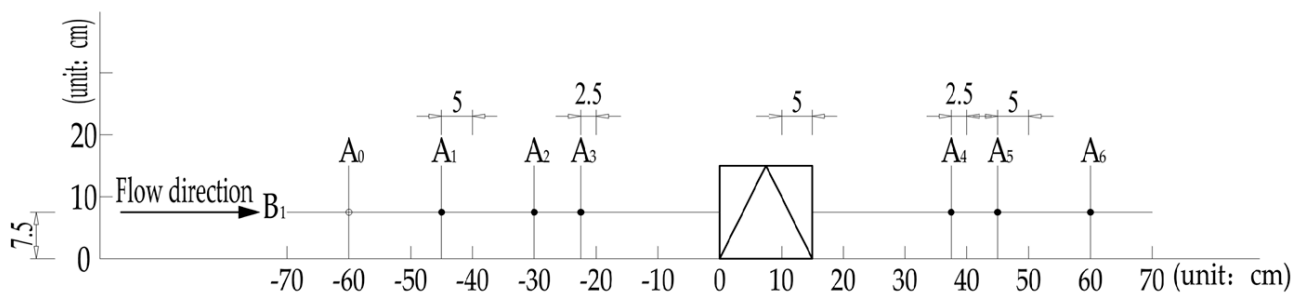**Figure 2.** Installation schematic diagram of the single model.

Figure 3. Schematic diagram of the locations of measurement points (section y = 7.5 cm).

2.3. Numerical Calculation

Because of their wide range of applications, numerical flow calculations ("computational fluid dynamics" or "CFD" for short) are popular tools to reflect the flow vortex and flow fields outside the artificial reefs. The cornerstone of the CFD is the fundamental governing equations of fluid dynamics—the continuity, momentum and energy equations [29]. Turbulence is an irregular and unpredictable fluid movement, which is usually caused by irregular parts such as velocity and density. In this paper, the fluid passing artificial reef is turbulent, so a turbulence model is used.

In this study, the Reynolds-averaged Navier–Stokes equations (RANS equations) are used to describe the viscous flows. We discretized the RANS equations in space using a finite volume method (FVM). The RNG model has an additional term in its ε equation that improves the accuracy for rapidly strained flows. The effect of swirl on turbulence is included in the RNG model, enhancing the accuracy for swirling flows. The RNG theory provides an analytical formula for turbulent Prandtl numbers, while the standard $k-\varepsilon$ model uses user-specified, constant values. While the standard $k-\varepsilon$ model is a high-Reynolds number model, the RNG theory provides an analytically derived differential formula for effective viscosity that accounts for low-Reynolds number effects. Effective use of this feature does, however, depend on an appropriate treatment of the near-wall region. These features make the RNG $k-\varepsilon$ model more accurate and reliable for a wider class of flows than the standard model. In this way, the accuracy of the flow fields around the submerged complex geometry was improved [30].

2.3.1. Governing Equations and Turbulence Model

Based on the flow motion characteristics in the vicinity of artificial reefs, in order to improve the efficiency of the calculations on 3D turbulence performance, the water flow in the numerical model is assumed to be an incompressible and viscous Newtonian fluid without heat exchange in an unsteady state. The continuity equation in Cartesian space and the Reynolds-averaged Navier–Stokes equations are as follows:

$$\frac{\partial u_i}{\partial x_i} = 0 \tag{1}$$

$$\frac{\partial u_i}{\partial t} + \frac{\partial u_j u_i}{\partial x_i} = -\frac{\partial p}{\partial x_i} + \frac{\partial}{\partial x_j}(\mu \frac{\partial u_i}{\partial x_j} - \overline{u_i'u_j'}) + f_i \qquad (2)$$

where p is the average pressure; u_i is the mean speed at x, y, z; μ is the viscidity; $\overline{u_i'u_j'}$ is the Reynolds stress and $i, j = 1, 2, 3$ (x, y, z) in the equation above. The flow field of the artificial reef was simulated using the Fluent software 16.0, and the control equation was solved using the finite volume method.

As the flow will abruptly change its magnitude and direction, the RNG $k - \varepsilon$ turbulence model was modified to address the turbulence closure. This can better simulate the flow in the near-wall area and with a low Reynolds number.

$$\frac{\partial(\rho k)}{\partial t} + \frac{\partial(\rho k u_i)}{\partial x_i} = \frac{\partial}{\partial x_j}\left(\alpha_k \mu_{eff}(\frac{\partial k}{\partial x_j})\right) + G_k + \rho\varepsilon \qquad (3)$$

$$\frac{\partial(\rho\varepsilon)}{\partial t} + \frac{\partial(\rho\varepsilon u_i)}{\partial x_i} = \frac{\partial}{\partial x_j}\left(\alpha_\varepsilon \mu_{eff}(\frac{\partial\varepsilon}{\partial x_j})\right) + \frac{C_{1\varepsilon}^*\varepsilon}{k}G_k - C_{2\varepsilon}\rho\frac{\varepsilon^2}{k} \qquad (4)$$

where μ_{eff} represents the effective viscosity factor $\mu_{eff} = \mu + \mu_t$; μ_t represents the turbulent viscosity factor $\mu_t = \rho C_\mu \frac{k^2}{\varepsilon}$. The turbulent kinetic energy (G_k) due to the average velocity gradient is represented as follows: $G_k = 2\mu_t E_{ij}E_{ij}$, $E_{ij} = \frac{1}{2}\left(\frac{\partial u_i}{\partial x_j} + \frac{\partial u_j}{\partial x_i}\right)$, and $C_{1\varepsilon}^* = C_{1\varepsilon} - \frac{\eta(1-\eta/\eta_0)}{1+\beta\eta^3}$; the values of C_μ, $C_{1\varepsilon}$, and $C_{2\varepsilon}$ are 0.085, 1.42, and 1.68, respectively.

2.3.2. Structure of the Artificial Reef and Computational Domain

In this article, the length (L), width (W), and height (H) of the reef are $3.0 \times 3.0 \times 30$ m, respectively. The models were constructed using Gambit and a computational domain with $11L \times 6W \times 5H$. Another cuboid domain of $5L \times 3W \times 3H$ was inserted between the coral reef and the computational domain to achieve the purpose of encrypting the local grids around the coral reef. This reduced the number of calculations and the results were more precise. The bottom center of the reef model, which was intended to serve as the coordination origin, was placed $4L$ downstream of the velocity inlet, as shown Figure 4. The outflow was designated to be on the backside, where the pressure was uniform and the gradient for all variables was zero. The wall surface of the flume and artificial reefs was prescribed as the stationary no-slip boundary condition. The model's surfaces and bottom side were thought to be smooth walls. For spatial discretization, the quadratic upwind interpolation (QUICK) approximation was chosen. The semi-implicit method for pressure-linked equations consistent (SIMPLEC) method was used to iterate the equations in the stable state. As soon as the residuals were below 10^{-5}, convergence was assumed.

2.3.3. Grid Convergence Verification

The independence analysis of the mesh is given in Section 2.3.3, the computational time is also included for the simulations in Table 1. To reduce the error caused by different grid sizes, this study selected a reef with a COR of 0.1 and a flow velocity of 0.8 m/s for the simulation. The grid size of the encrypted domain was 0.300 m, and that of the non-encrypted domain, which was set for four different groups, was larger than 0.300 m. Table 1 shows the results.

As shown in Table 1, when the element size is 0.500 m, the reef will have a more stable drag coefficient and a better element number and convergence. The element size of the encrypted domain was 0.300 m, while for the others were 0.500 m. Moreover, the flow velocity was 0.8 m/s, which is the typical speed of waters in Shandong Province, China.
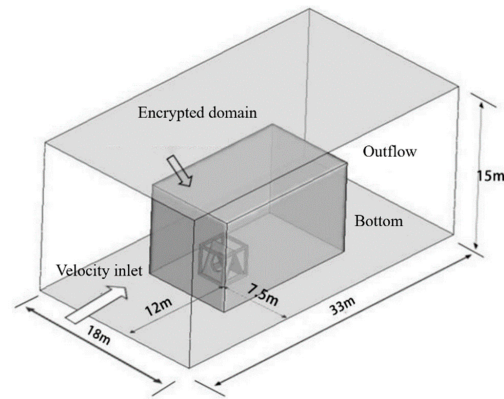
Figure 4. The simulation domain of the model (unit: m).

Table 1. Results of the simulation.

Computational Time (h)	Size of the Max Grid (m)	Number of Grids ($\times 10^5$)	Drag Coefficient
2.4	0.900	1.089	1.966
11.0	0.700	2.263	1.915
30.5	0.500	6.170	1.916
64.8	0.300	28.419	1.900

2.3.4. Verification of Model Reliability

To test the reliability of the simulation model, we conducted an experiment with different CORs and flow velocities corresponding to the conditions used in the simulation model. The comparison between the experiment and simulation is displayed in Figure 5.
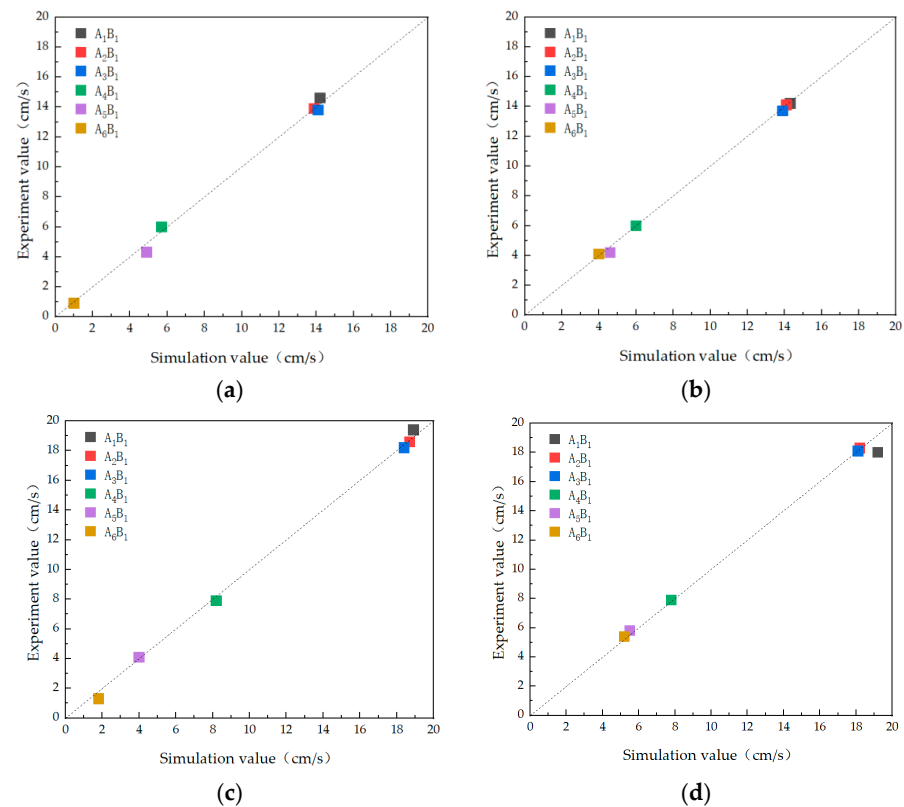

Figure 5. Comparison of the results between the simulation and experiment with different velocities and CORs. (**a**) $\varphi = 0.1$; v = 0.6 m/s. (**b**) $\varphi = 0.2$; v = 0.6 m/s. (**c**) $\varphi = 0.1$; v = 0.8 m/s. (**d**) $\varphi = 0.2$; v = 0.8 m/s.

The above figure shows that the comparison with different flow velocities and the two CORs are in good agreement when the flow velocity and COR are larger. The errors at points A_4B_1 and A_5B_1 were larger with values of 12.31 and 9.36%, respectively, because the vortex phenomenon easily appears behind the reef when the flow velocity and COR are 0.6 m/s and 0.1, respectively. The data fit better with a flow velocity of 0.6 m/s and a COR of 0.1, and only a larger error of 11.67% appears at A_4B_1. Notably, most measurement points show good agreement, confirming the simulation flume's credibility.

3. Results and Discussion

The effect of the reef can be reflected by the upwelling and rear vortex field. The horizontal flow velocity of the back vortex field and upwelling is less than 0, while the ratio of the field's vertical velocity to horizontal velocity is no less than 5%. The reef with cut-opening makes the flow field more complex, which can provide better conditions for fish growth. The COR represents the cut-opening projection area in the flow upstream face perpendicular to the flow direction. The flow velocity (u) must be taken into account when choosing the site for the reef because this can influence the distribution of the flow field, and thus affect the artificial reef's stability. In this study, the hydrodynamic field and drag coefficient were studied with five different opening ratios (0, 0.1, 0.2, 0.3, and 0.4) and five different flow velocities (0.2, 0.4, 0.5, 0.6, and 0.8 m/s) in the simulation.

3.1. Hydrodynamic Field Analysis

(1) Using u = 0.5 m/s as an example, the hydrodynamic characteristics were simulated for the square reef without an upwelling plate and with opening ratios of 0, 0.1, 0.2, 0.3, and 0.4.

As shown in Figure 6 and Table 2, the flow field around the DCAR is more complex compared to that around the ordinary cubic artificial reef (OCAR), and its upwelling characteristic parameters are much better. The maximum upwelling volume of the DCAR is 16.73 times that of the OCAR.

Table 2. Upwelling characteristic parameters with different cut-opening ratios.

Type of Reef	Cut-Opening Ratio (φ)	Maximum Height of Upwelling/Reef Height (H_{u-max}/H)	Upwelling Horizontal Span/Reef Length (L_{u-max}/L)	Vertical Maximum Velocity Component/ Inflow Velocity (V_{z-max}/V)	Volume of Upwelling/ Volume of Reef (V_{max}/V)
OCAR	/	1.48	1.66	0.35	0.67
DCAR	0.00	2.69	5.50	0.69	11.24
	0.10	2.56	5.67	0.82	9.05
	0.20	2.44	5.94	0.58	8.13
	0.30	2.31	6.24	0.53	7.03
	0.40	2.16	6.85	0.40	4.96

When the COR increases from 0 to 0.3, the upstream face of the reef can block the flow to varying degrees. A certain domain is formed close to the front and rear of the reef where the velocity is slightly lower than the inflow velocity. Alternatively, the domain with a velocity higher than the inflow appears above the reef, which becomes smaller with a larger COR. When the COR is larger than 0.3, the supercritical flow domain gradually disappears above the reef. When the COR is between 0.2 and 0.3, the subcritical flow domain behind the reef becomes smaller, and is largest with a COR of 0.2. The upwelling domain is largest without the cut-opening, but the horizontal span and vertical velocity of the upwelling are smaller than those of the reef with a COR of 0.1, which accelerates the flow between the reefs. Therefore, the reef has a better hydrodynamic field characteristic when the COR is 0.1–0.2.

According to Figure 7, when COR is 0–0.2, a counterclockwise vortex is formed behind the reef, greatly blocking the flow. When the COR is higher than 0.2, the permeability in the middle of the riser increases. Moreover, the velocity vector tends to be

parallel, and the vortex region disappears. As seen in Table 3, at a speed of 0.5 m/s, the OCAR does not display a back vortex, but the DCAR does. DACR shows that different sizes of back vortex surround the reef. As the COR rises, the back vortex's horizontal width and volume gradually shrink. When the COR reaches 0.1, the height of the back vortex becomes 1.21 times higher than the reef's height, while its horizontal span is 2.55 times larger than the reef's length.
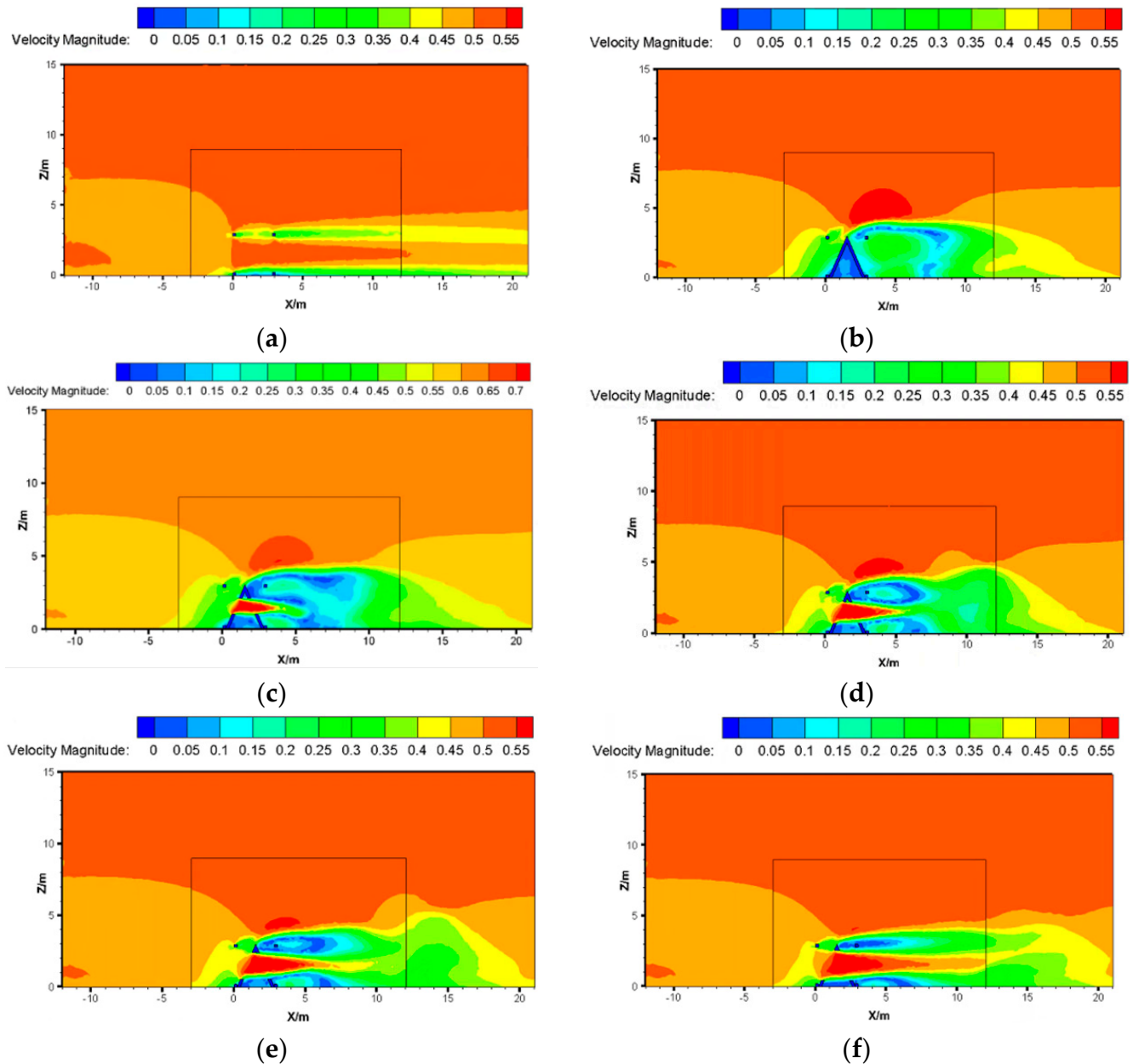

Figure 6. Velocity contour of the longitudinal central axis section. (**a**) Without diversion plate. (**b**) φ = 0.0. (**c**) φ = 0.1. (**d**) φ = 0.2. (**e**) φ = 0.3. (**f**) φ = 0.4.

(2) The following tables and figures show the hydrodynamic parameters with a COR of 0.1 and under different flow velocities (0.2, 0.4, 0.5, 0.6, and 0.8 m/s):

Figure 8 and Table 4 show that as the flow velocity increases, the domains of the subcritical flow and supercritical flow become larger, and the height, horizontal span, and volume of the upwelling also tends to increase. The maximum values of the parameters are reached when the velocity is 0.8 m/s. In addition, the velocity's vertical component does not change significantly.
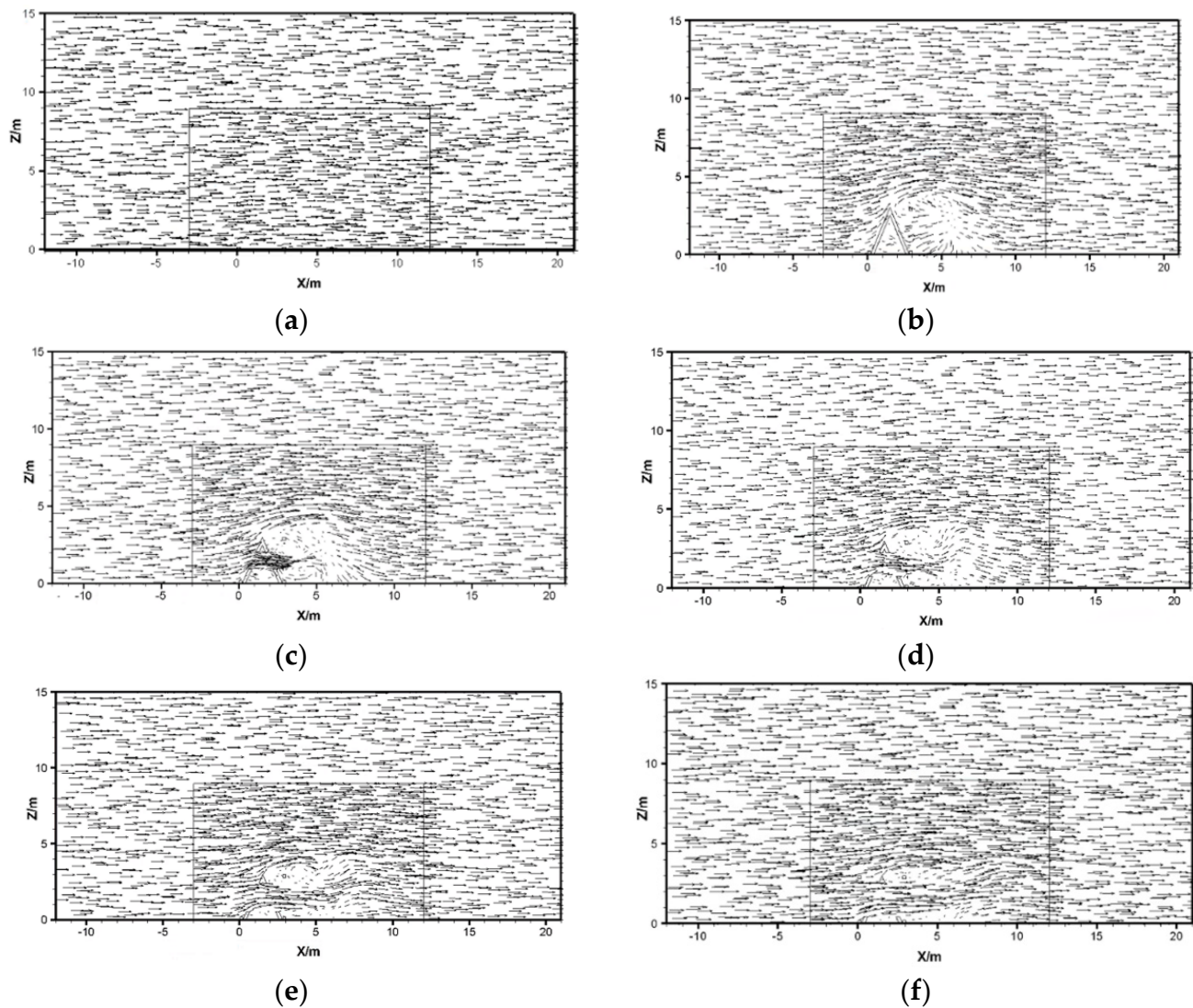
(a)

(b)

(c)

(d)

(e)

(f)

Figure 7. Velocity vector distribution of the longitudinal central axis section. (**a**) Without diversion plate. (**b**) φ = 0.0. (**c**) φ = 0.1. (**d**) φ = 0.2. (**e**) φ = 0.3. (**f**) φ = 0.4.

Table 3. Vortex characteristic parameters with different cut-opening ratios.

Type of Reef	Cut-Opening Ratio (φ)	Maximum Height of Back Vortex/Reef Height (H_{v-max}/H)	Back Vortex Horizontal Span/Reef Length (L_{v-max}/L)	Back Vortex Horizontal Width/Reef Width (W_{max}/W)	Volume of Back Vortex /Reef Volume (V_{max}/V)
OCAR	/	0	0	0	0
DCAR	0	1.19	2.47	1.09	1.03
	0.10	1.21	2.55	1.05	0.62
	0.20	1.14	1.90	0.98	0.31
	0.30	1.14	1.87	0.90	0.16
	0.40	1.07	1.67	0.83	0.03

According to Figure 9, when the flow velocity increases, the turbulence state becomes more complex, but its position remains unchanged. According to Table 5, which shows the parameters of the vortex, changes in the flow velocity do not affect the height and horizontal width of the back vortex, which stay at 1.20 times and 1.05 times greater than those of the reef, respectively. However, the value of the flow velocity will influence the

horizontal span and volume of the back vortex. Thus, we can conclude that a higher velocity can generate a better result.
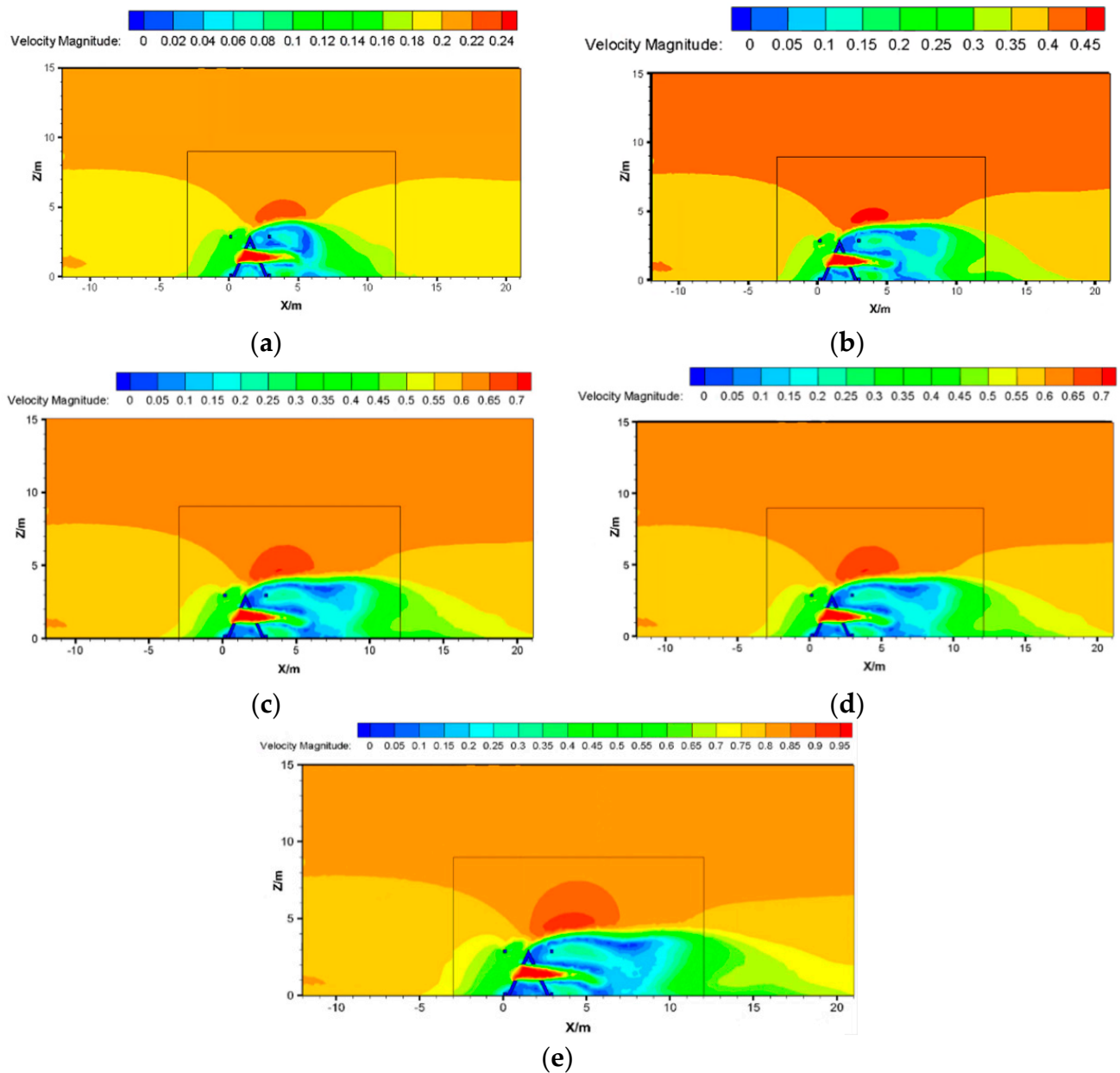

Figure 8. Velocity contour of the longitudinal central axis section. (**a**) u_1 = 0.2 m/s. (**b**) u_2 = 0.4 m/s. (**c**) u_3 = 0.5 m/s. (**d**) u_4 = 0.6 m/s. (**e**) u_5 = 0.8 m/s.

Table 4. Upwelling characteristic parameters with different flow velocities.

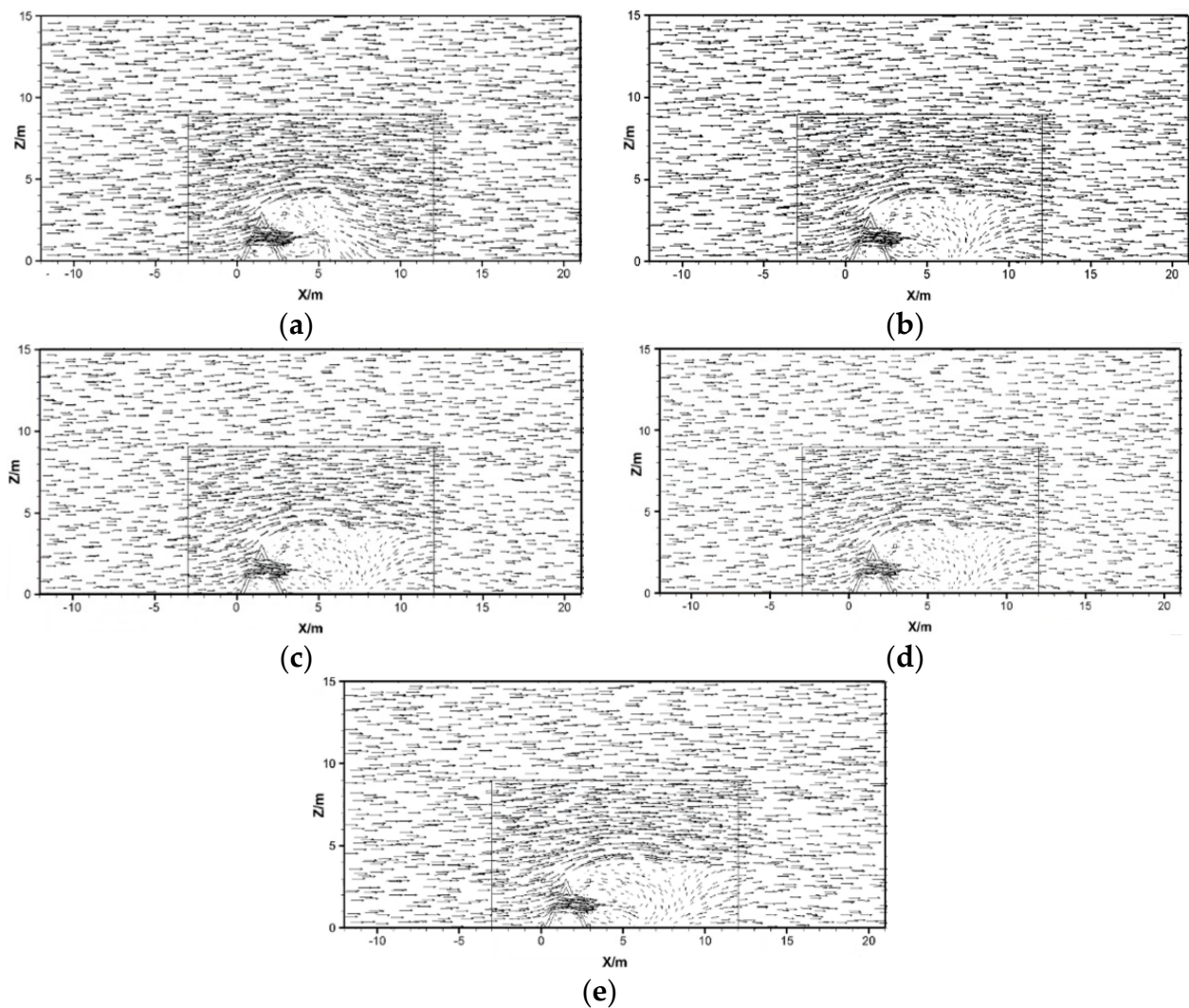| Flow Velocity (m/s)	Maximum Height of Upwelling/ Reef Height ($H_{u-\max}/H$)	Upwelling Horizontal Span/Reef Length ($L_{u-\max}/L$)	Vertical Maximum Velocity Component/Inflow Velocity ($V_{z-\max}/V$)	Volume of Upwelling/ Volume of Reef ($V_{\max}/V$)
0.2	2.45	3.59	0.73	7.23
0.4	2.56	5.18	0.70	9.05
0.5	2.56	5.67	0.82	9.05
0.6	2.56	5.68	0.69	9.49
0.8	2.63	5.99	0.69	9.86

Figure 9. Velocity vector distribution of the longitudinal central axis section. (**a**) $u_1 = 0.2$ m/s. (**b**) $u_2 = 0.4$ m/s. (**c**) $u_3 = 0.5$ m/s. (**d**) $u_4 = 0.6$ m/s. (**e**) $u_5 = 0.8$ m/s.

Table 5. Vortex characteristic parameters with different flow velocities.

Flow Velocity (m/s)	Maximum Height of Back Vortex/Reef Height (H_{v-max}/H)	Back Vortex Horizontal Span/Reef Length (L_{v-max}/L)	Back Vortex Horizontal Width/Reef Width (W_{max}/W)	Volume of Back Vortex /Reef Volume (V_{max}/V)
0.2	1.20	1.69	1.00	0.33
0.4	1.20	2.43	1.05	0.57
0.5	1.21	2.55	1.05	0.62
0.6	1.21	2.55	1.05	0.61
0.8	1.21	2.70	1.05	0.67

3.2. Drag Coefficient

In the fluent, one artificial reef is generally subjected to forces in the stream-wise and transverse direction, which are called the drag force and lift force, respectively. The coefficient related to the drag force is the drag coefficient. The drag coefficient can be calculated from the formula below:

$$C_d = \frac{F}{\frac{1}{2}\rho A u^2} \tag{5}$$

where *F*—drag force, *A*—area of reef facing the flow, ρ—the density, and *u*—flow velocity.

The stability of the reef on the seabed is mainly determined by the drag force caused by the flow, and the drag coefficient is an important characteristic parameter of the drag force. In this article, the drag coefficient is calculated under the condition with a constant flow velocity.

Figure 10 displays the results of the correlation between the drag coefficient and the COR when the flow velocities are 0.2 m/s, 0.4 m/s, 0.5 m/s, 0.6 m/s, and 0.8 m/s. When the flow velocity is between 0.2 m/s and 0.4 m/s, the drag coefficient clearly decreases. The drag coefficient tends to level off with flow velocities greater than 0.4 m/s. When the opening ratio φ is 0–0.4, the drag coefficient increases and then decreases with increasing COR; the largest result was obtained with a COR of 0.2.
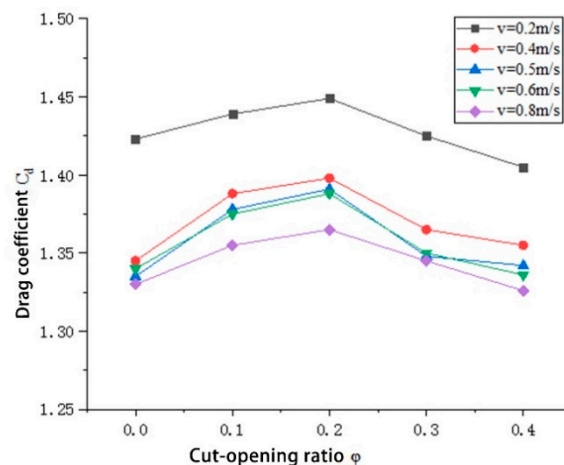

Figure 10. The relationship between the drag coefficient and COR.

4. Conclusions

The flow field effect is an influential factor on the ecological footprint. A well-designed artificial reef has a positive impact on the flow field. Typically, the artificial reef is designed to have holes on both sides, but its design principle is still unclear. To analyze the artificial reef's flow field effects, this study used COR and flow velocity as two parameters. The outcomes show that a diversion can improve the flow characteristics of square-shaped artificial reefs.

The upwelling and back vortex parameters generated by the reef increase with increasing flow velocity and decrease with increasing COR. When the COR and flow velocity are at 0 m/s and 0.8 m/s, respectively, the volume of the upwelling reaches a maximum. However, when COR was 0, it was too small to facilitate the exchange of flow inside the reef. When the COR was 0.1–0.2, the flow field produced the best results. The drag coefficient of the reef decreased when the flow velocity was between 0.2 m/s and 0.4 m/s, but when the velocity exceeded 0.4 m/s, the coefficient leveled out. When the COR was 0–0.4, the drag coefficient rose and subsequently fell. When the COR was 0.2, drag coefficient reached a maximum. When optimizing the design of a reef, the COR should be kept within 0.1–0.2. At the location of the reef, the flow velocity should be 0.5–0.8 m/s. When the conditions are met, the parameters, such as upwelling and the back vortex of a single reef, are better and the flow field impact is adequate.

Author Contributions: Methodology, H.M.; Validation, C.H.; Formal analysis, Z.W. and K.W.; Writing—original draft, H.M.; Writing—review & editing, H.M. All authors have read and agreed to the published version of the manuscript.

Data Availability Statement: The data presented in this study are available on request from the corresponding author.

Conflicts of Interest: The authors declare no conflict of interest.

References

1. Genzano, G.; Giberto, D.; Bremec, C. Benthic survey of natural and artificial reefs off Mar del Plata, Argentina, southwestern Atlantic. *Lat. Am. J. Aquat. Res.* **2011**, *39*, 553–566. [CrossRef]
2. Farinas-Franco, J.M.; Allcock, L.; Smyth, D.; Roberts, D. Community convergence and recruitment of keystone species as performance indicators of artificial reefs. *J. Sea Res.* **2013**, *78*, 59–74. [CrossRef]
3. Farinas-Franco, J.M.; Roberts, D. Early faunal successional patterns in artificial reefs used for restoration of impacted biogenic habitats. *Hydrobiologia* **2014**, *727*, 75–94. [CrossRef]
4. Walles, B.; Troost, K.; van den Ende, D.; Nieuwhof, S.; Smaal, A.C.; Ysebaert, T. From artificial structures to self-sustaining oyster reefs. *J. Sea Res.* **2016**, *108*, 1–9. [CrossRef]
5. Perkol-Finkel, S.; Zilman, G.; Sella, I.; Miloh, T.; Benayahu, Y. Floating and fixed artificial habitats: Effects of substratum motion on benthic communities in a coral reef environment. *Mar. Ecol. Prog. Ser.* **2006**, *317*, 9–20. [CrossRef]
6. Gallaway, B.J.; Szedlmayer, S.T.; Gazey, W.J. A life history review for red snapper in the Gulf of Mexico with an evaluation of the importance of offshore petroleum platforms and other artificial reefs. *Rev. Fish. Sci.* **2009**, *17*, 48–67. [CrossRef]
7. Dance, M.A.; Patterson, W.F.; Addis, D.T. Fish community and trophic structure at artificial reef sites in the northeastern Gulf of Mexico. *Bull. Mar. Sci.* **2011**, *87*, 301–324. [CrossRef]
8. Becker, A.; Taylor, M.; Folpp, H.; Lowry, M. Revisiting an artificial reef after 10 years: What has changed and what remains the same. *Fish. Res.* **2022**, *249*, 106261. [CrossRef]
9. Herrera Pérez, R.B. Dinámica de las Comunidades Bentónicas de los Arrecifes Artifificiales de Arguineguín (Gran Canaria) yLanzarote. Ph.D. Thesis, Facultad de Ciencias del Mar, Puerto Real, Spain, 1998.
10. Carral, L.; Lamas, M.I.; Cartelle Barros, J.J.; López, I.; Carballo, R. Proposed conceptual framework to design artificial reefs based on particular ecosystem ecology traits. *Biology* **2022**, *11*, 680. [CrossRef]
11. Liu, Y.; Guan, C.T.; Zhao, Y.P.; Cui, Y.; Dong, G.H. Numerical simulation and PIV study of unsteady flow around hollow cube artificial reef with free water surface. *Eng. Appl. Comp. Fluid.* **2012**, *6*, 527–540. [CrossRef]
12. Jiang, Z.Y.; Liang, Z.L.; Zhu, L.X.; Liu, Y. Numerical simulation of effect of guide plate on flow field of artificial reef. *J. Ocean. Eng.* **2016**, *116*, 236–241. [CrossRef]
13. Li, J.; Zhang, S.Y. The comparison between numerical simulation and water channel experiment on Mi zi artificial reef. *J. Fish. China* **2010**, *34*, 1587–1594. [CrossRef]
14. Lan, X.Z.; Wan, R.; Tang, Y.L.; Huang, L.Y.; Zhao, F.F.; Bao, W.G.; Liu, C.D.; Wang, Z.L. Numerical simulation of the flow field around the truncated-cone shaped artificial reef. *J. Period. Ocean. Univ. China* **2016**, *46*, 47–53.
15. Yu, D.Y.; Zhao, W.; Wang, F.Y.; Wang, S.L. Trapezoid artificial reefs in different deployment spacing: Physical and numerical simulation. *J. Oceanol. Limnol. Sin.* **2020**, *51*, 283–292.
16. Huang, Y.D.; Fu, D.F.; He, W.R. Three dimensional numerical simulation on influence of COR of artificial reef on flow effect. *J. Water Resour. Water Eng.* **2014**, *25*, 39–43.
17. Wang, G.; Wan, R.; Wang, X.X.; Zhang, F.F. Study on the influence of COR, cut-opening shape, and cut-opening number on the flow field of a cubic artificial reef. *J. Ocean. Eng.* **2018**, *162*, 341–352. [CrossRef]
18. Jiang, Z.Y.; Liang, Z.L.; Zhu, L.X.; Guo, Z.S.; Tang, Y.L. Effect of hole diameter of rotary-shaped artificial reef on flow field. *J. Ocean. Eng.* **2020**, *197*, 106917. [CrossRef]
19. Tang, Y.L.; Yang, W.Z.; Sun, L.Y.; Zhao, F.F.; Long, X.Y.; Wang, G. Studies on factors influencing hydrodynamic characteristics of plates used in artificial reefs. *J. Ocean. Univ. China* **2019**, *18*, 193–202. [CrossRef]
20. Guo, Y.; Zhang, S.Y.; Lin, J. Flow field efficiency of Mi-zi artificial reefs in different construction modes based on numerical experiments. *J. Fish. China* **2019**, *43*, 2025–2038.
21. Zhou, P.Y.; Gao, Y.Y.; Zheng, S. Three-dimensional numerical simulation on flow behavior behind trapezoidal artificial reefs. *Ocean. Eng.* **2022**, *266*, 112899. [CrossRef]
22. Wei Jiang, C.B.; Yunpeng, Z.; Yong, C. Numerical simulation of hydrodynamic characteristics of hollow artificial reef in wave-current. *Fish. Mod.* **2017**, *44*, 30–37.
23. Nie, Z.; Zhu, L.; Xie, W.; Zhang, J.; Wang, J.; Jiang, Z.; Liang, Z. Research on the influence of cut-opening factors on flow field effect of artificial reef. *Ocean. Eng.* **2022**, *249*, 110890. [CrossRef]
24. Wang, X.; Liu, X.; Tang, Y.; Zhao, F.; Luo, Y. Numerical Analysis of the Flow Effect of the Menger-Type Artificial Reefs with Different Void Space Complexity Indices. *Symmetry* **2021**, *13*, 1040. [CrossRef]
25. Galdo, M.I.L.; Guerreiro, M.J.R.; Vigo, J.L.; Rodriguez, I.A.; Lorenzo, R.V.; Couce, J.C.C.; Couce, L.C. Definition of an Artificial Reef Unit through Hydrodynamic and Structural (CFD and FEM) Models—Application to the Ares-Betanzos Estuary. *J. Mar. Sci. Eng.* **2022**, *10*, 230. [CrossRef]
26. Liu, H.S.; Ma, X.; Zhang, S.Y.; Yu, H.B.; Huang, H.J. Research on model experiments of effects of artificial reefs on flow field. *J. Fish. China* **2009**, *33*, 229–236.

27. Zhang, S.; Zhang, S.D.; Chu, W.H.; Hu, F.X. Model experiment of hydrodynamic performance of square artificial reefs with hexagonal openings. *J. Fish. China* **2020**, *44*, 1903–1912.
28. Fu, D.W.; Chen, Y.; Chen, Y.S.; Luan, S.G. PIV experiment of artificial monomer reefs on the flowing field. *J. Dalian Fish. Univ.* **2014**, *29*, 82–85.
29. Anderson, J.D. *Computational Fluid Dynamics*; McGraw-Hill Inc.: New York, NY, USA, 1995.
30. Liu, T.L.; Su, D.T. Numerical analysis of the influence of reef arrangements on artificial reef flow fields. *Ocean Eng.* **2013**, *74*, 81–89. [CrossRef]